Nanoscale

COMMUNICATION

View Article Online
View Journal | View Issue

Cite this: *Nanoscale*, 2025, **17**, 17057

Received 6th March 2025,
Accepted 30th June 2025

DOI: 10.1039/d5nr00983a

rsc.li/nanoscale

Radiofrequency-triggered release of therapeutics from graphene oxide-loaded polysaccharide based core–shell microspheres†

Aiswarya Thattaru Thodikayil,‡[a] Agni Kumar Biswal,‡[b] Aniruddh Vashisth [b] and Sampa Saha *[a]

Triggered drug delivery systems have revolutionized the administration of therapeutics by enabling precise and controlled release. Herein, we present radiofrequency (RF)-responsive core–shell microsphere systems composed of acetalated dextran (Ac-D) and carboxymethyl nanocellulose (CMC) integrated with nanoscale graphene oxide (GO) and encapsulating curcumin as a model drug. These hybrid systems leverage the RF-absorbing properties of carbon-based nanomaterials, specifically GO, which acts as a nanoscale thermal transducer within the microscale carriers. Upon exposure to a reduced RF input (1–7 watts), 1–200 MHz, localized heating induced by embedded GO facilitated the release of the encapsulated drug. Drug release kinetics revealed over 98% curcumin release within 60 minutes under RF stimulation with minimal passive release in its absence, confirming the structural stability of the microspheres under physiological conditions. The RF-triggered release mechanism was further supported by swelling behavior (~60–70%) and surface charge differences in GO-loaded particles, indicating enhanced water penetration and matrix disruption. These findings establish the nanoscale integration of GO as a key enabler for non-invasive, RF-triggered drug delivery, offering spatiotemporal control. This system holds promises for future biomedical applications, particularly for topical and localized therapy, and warrants further investigation through *in vivo* studies.

1. Introduction

Effective triggered drug delivery remains a significant challenge due to the lack of precision, stability, and efficacy in existing drug carrier systems for treating complex diseases such as cancer, diabetes, arthritis, stroke, and asthma.[1–6] This underscores the need for advanced drug delivery systems such as smart carriers, designed to address these shortcomings. Research on smart carriers has primarily focused on improving drug efficacy and diffusion by optimizing the matrices used while minimizing side effects.[7–9] These systems often require specific conditions, such as internal stimuli (*e.g.*, pH, enzymes, or redox gradients)[10] or external triggers (*e.g.*, magnetic fields, light, temperature, or high-energy radiation),[11] to achieve controlled 'on-demand' drug release (Table S1†).[12] Among these, external stimuli are more commonly used for invasive treatment when rapid intervention is necessary. In particular, electromagnetic fields, and more specifically radiofrequency (RF) waves, have emerged as promising triggers for externally controlled drug release.

RF-triggered drug delivery offers an innovative solution to overcome major limitations of conventional systems, such as uncontrolled biodistribution, off-target release, and systemic toxicity.[13,14] This innovative approach offers a way to address the limitations of conventional drug delivery methods, such as systemic side effects from off-target release, uncontrolled drug distribution, nonspecific biodistribution, and adverse reactions due to overdose.[15,16] However, for RF-induced heating and drug release to be effective, specific materials like graphene oxides (GO) nanosheet, gold nanoshells[17] or graphitic carbon[18] are required within the system to absorb the RF energy and transfer it to the drug carrier.[19,20] Unlike other carbon-based nanomaterials, such as carbon nanotubes (CNTs), GO is highly dispersible in aqueous media due to its abundant oxygen-containing functional groups (*e.g.*, hydroxyl, carboxyl, and epoxy), that facilitates its integration into hydrophilic polymer matrices like acetalated dextran and carboxymethyl cellulose. These functional groups not only enhance its biocompatibility but also enable non-covalent interactions with therapeutic molecules, improving drug loading and stability.[21] Moreover, GO has been shown to possess efficient RF and photothermal energy absorption properties due to its 2D structure and delocalized π-electron system, making it an excel-

[a]*Department of Materials Science and Engineering, Indian Institute of Technology Delhi, New Delhi, 110016-India. E-mail: Sampa.Saha@mse.iitd.ac.in*
[b]*Department of Mechanical Engineering, University of Washington, Seattle, 98195-USA*

†Electronic supplementary information (ESI) available. See DOI: https://doi.org/10.1039/d5nr00983a

‡These authors made equal contributions to this paper.

lent nanoscale thermal transducer.[22] Compared to CNTs, which often require complex surface functionalization to achieve biocompatibility and dispersion, GO provides a safer and more readily processable alternative for biomedical applications.[23,24] To improve GO's long-term performance, physiological stability, and biocompatibility, it is often coated with biocompatible polymers. Sasidharan *et al.*[25] studied the use of carboxylated graphene for RF-induced hyperthermia to target radiation-resistant cancer cells (K562R). By conjugating transferrin, an iron-transport protein to carboxyl-functionalized graphene, they enhanced RF absorption and thermal conductivity, ultimately causing cancer cell death. However, one major concern with modified graphene systems is their limited biodegradability, which can lead to long-term toxicity and hinder their clinical translation.[26,27] In another study, Koyakutty *et al.*[28] developed RF-responsive stannous-doped alginate nanoparticles loaded with doxorubicin and coated with polyethylenimine (PEI). These particles, designed for both RF-induced thermal ablation and drug release, showed potential for treating liver tumors.[28] Traditional RF therapy often requires high power (>100 W) over extended periods, which can result in healthy cell damage and significant side effects.[29–32] Several studies also indicates that graphene oxide (GO) exhibits low toxicity at appropriate doses, particularly when embedded within a biocompatible matrix. For instance, Liao *et al.* demonstrated minimal cytotoxicity of GO at concentrations below 50 μg mL^{-1}.[33] Similarly, Fadeel *et al.* highlighted that rational surface engineering and matrix encapsulation can significantly enhance its safety profile.[34] Based on these insights, we sought to investigate electromagnetic heating methods that require minimal RF power, incorporating GO at concentrations below 50 μg mL^{-1} in our system to ensure biocompatibility.

Multi-layered microparticles, such as core–shell or bicompartmental particles, are particularly well-suited for the controlled and sustained release of drugs when coupled with appropriate stimuli for topical applications.[35,36] Drug carrier systems with a core–shell structure have demonstrated significant potential in providing precise and prolonged drug release. Conventional topical delivery platforms frequently exhibit inadequate retention at the target location, uncontrolled drug release, and restricted skin penetration which reduces their therapeutic efficacy. Through our study we have attempted to address these constraints. The core shell architecture of microspheres offers drug stability and prevents its premature release. Also, the larger size enables localized depot formation on surface of the skin, improving the site-specific retention and lowering the systemic absorption. Above all, the RF-triggered release mechanism facilitates the on-demand cancer drug administration under external control thereby regulating the drug release in response to therapeutic needs. This feature enhances the precision and effectiveness of the proposed therapeutic strategy by addressing several limitations associated with conventional topical delivery systems. Polysaccharide derivatives like acetalated-dextran, cellulose *etc.* are ideal due to their biocompatibility, high degradability, and non-toxic nature, making them highly adaptable for biomedical applications.[37] Therefore, utilizing a matrix system composed of acetalated-dextran and cellulose, created through a simple double emulsion technique appears to be promising. A combination of dextran derivative, widely used in pharmaceutical drug carriers, and cellulose, known for its high porosity and surface area, can be considered as excellent candidates as core–shell drug carriers for enhancing the treatment outcome.[38,39]

Curcumin, a hydrophobic polyphenolic compound, is widely recognized for its potent anticancer activity against various cancer cell types such as skin,[40] prostate[41] and breast cancer.[42] Numerous studies have shown that curcumin induces apoptosis by targeting multiple molecular signaling pathways and effectively inhibits critical steps in cancer progression, including metastasis, and angiogenesis. However, it is challenging to broaden the utilization of it considering its poor aqueous solubility, limited systemic bioavailability, and rapid elimination from the body. To overcome these limitations, we have employed curcumin as a model therapeutic agent to evaluate the performance of our RF triggered responsive drug delivery system. To further render the system responsive to external stimuli, graphene oxide (GO) was incorporated into the drug carriers. Among the various RF-responsive materials discussed, GO is particularly effective in absorbing radiofrequency waves and generating heat even at low power inputs. This is due to the presence of monolayer sp^2 hybridized carbon and disruptions in the π-electron cloud within these carbonaceous structures.[43] Numerous studies have highlighted the biocompatibility of graphene derivatives for various biomedical applications.[44,45] Therefore, incorporating GO into a biodegradable polysaccharide-based system enhances the responsiveness of the drug carriers to RF stimuli, offering a more advanced approach to electromagnetic field-triggered drug release.

Compared to previously reported studies, where the study has been conducted using kHz range and high power used for drug release;[46–48] herein we have used MHz (1–200) and a minimized RF power input of 1–10 watts (significantly lower than ~100 watts), to trigger drug release at a lower power range. This is certainly advantageous for a drug delivery system using RF as a trigger. We have designed and developed RF-responsive polysaccharide-based core–shell microspheres, incorporating graphene oxide and the model drug curcumin, using a double emulsion technique. The formation mechanism of these microspheres was examined through *in situ* tracking of their morphological properties. Through our study we have attempted to address the constraints of conventional topical delivery platforms such as inadequate retention at the target location, uncontrolled drug release, and restricted skin penetration which reduces their therapeutic efficacy. The core shell of architecture microsphere offers drug stability and prevents its premature release. Also, the larger size enables localized depot formation on surface of the skin, improving the site-specific retention and lowering the systemic absorption. Above all, the RF-triggered release mechanism facilitates the

on-demand cancer drug administration under external control thereby regulating the drug release in response to therapeutic needs. This feature enhances the precision and effectiveness of the proposed therapeutic strategy by addressing several limitations associated with conventional topical delivery systems.

2. Materials and methods

2.1. Materials

Dextran having a molecular weight, M_r (relative molecular mass) of 15 000–25 000 and polymeric blue dye (poly(9,9-di-*n*-octylfluorenyl-2,7-diyl), $M_w \geq 20\,000$) were bought from Sigma-Aldrich, India. Softwood pulp (94% alpha CMC, DP-870) was provided by Aditya Birla, India. Poly (vinyl alcohol) (PVA) (cold, M_w = 125 000 g mol^{-1}) was obtained from Chemical Drug House (CDH), India. Citric acid was procured from Fischer scientific USA. Polylactide (molecular weight: 40 000 g mol^{-1}) was obtained from Nature Work. Curcumin (>97.0% Purity) was purchased from TCI India. Dulbecco's Modified Eagle's medium (DMEM) and Fetal bovine serum (FBS) were purchased from HiMedia Laboratories India. MTT Cell Growth Assay Kit and Agarose were procured from Sigma-Aldrich India. HEK293 cell lines were purchased from National Centre for Cell Science (NCCS), Pune, India. The solubility of curcumin in various solvents is as follows, based on established literature: in water (~0.0004 mg mL^{-1}),[49] chloroform (~1.4 mg mL^{-1})[50] and dichloromethane (~0.88 mg mL^{-1}).[51]

2.2. Preparation of core shell constituents

2.2.1. Synthesis of acetalated dextran. Required precursor material for fabrication of micropshere, acetalated-dextran were synthesized following our previous work.[52] 1 g of dextran was charged into a flame dried round bottom flask and purged with N_2 for 1 h. Anhydrous DMSO (10 mL) was added to dissolve the dextran completely using a magnetic stirrer. After formation of a clear solution, pyridinium-*p*-toluene sulfonate (15.6 mg) was added to the solution, followed by the addition of 3.4 mL of 2-methoxypropene and continued the reaction for 3 h. The reaction was quenched by using 1 mL triethylamine. The resulting product was precipitated out in water and washed several times to remove any remaining salts and unreacted starting materials. The formation of acetalated-dextran was confirmed from ^{1}H NMR (Bruker Avance, 500 MHz, $CDCl_3$): 1.39 (s, br, 25H), 3.25 (br, 6H), 3.45 (br, 2H), 3.60–4.15 (br, 12H), 4.92 (br, 1H), 5.13 (br, 1H) (Fig. S1†).

2.2.2. Preparation of carboxy methyl cellulose (CMC). Carboxylated nano-fibrillated cellulose (CMC) having DP of 680 was prepared by following a published procedure.[53] This included the hydrolysis of pulp materials in aqueous citric acid (80) to yield CMC for 5 h using an overhead mechanical stirrer at 450 rpm.

2.2.3. Modification of graphene oxide (GO). The graphite powder was modified into the graphene oxide following Hummar's method.[54] Graphite powder (3 g) was dispersed in 140 mL of 98% H_2SO_4 under constant stirring and holding all set up under ice bath. To the resulted dark slurry, $NaNO_3$ (3 g) was gradually added. Subsequently, the mixture was brought to room temperature and stirred for an hour. Then, the mixture was stirred for 30 minutes at an elevated temperature of 80 °C following the addition of 250 mL of water. The above solution was further diluted by adding 800 mL of water and followed by slow addition of H_2O_2 to make them graphene oxides. The synthesized GO was washed multiple times with deionized water until the pH of the rinsing solution reached neutral.

2.3. Fabrication of core shell microspheres using emulsion techniques

The core/shell microspheres were fabricated from the acetalated-dextran and CMC, incorporating GOs into different phases using double emulsion technique. This follows the dispersion of CMC (600 mg) in an aqueous solution of 6 wt% NaOH (250 mg)/4 wt% urea (180 mg) in 5 mL of distilled water at low temperature (−50 °C) to form the water phase (W1). The preparation of oil phase (O) follows the dissolution of acetalated dextran (60 mg) in chloroform (450 μL). 160 μL of CMC solution from stock solution (W1) was slowly added to the oil phase followed by the probe sonication (1 min) to generate a homogenous water-in-oil emulsion. The resultant solution was poured into an external aqueous PVA solution of 250 mL (W2, 0.5 wt%) to form water (W1)–oil (O)–water (W2) and stirred under mechanical stirring (450 rpm) at 30 °C for 4 h. Before the formation of W1 in O, the GOs were added separately into the desired phase (either in core or in shell) and followed by one minute probe sonication to get good dispersion. The evaporation of solvent (chloroform) resulted in the formation of solid microspheres. The microspheres were collected by several washings with water, then lyophilized and stored for further characterization.

The drug loaded microparticles were also prepared following the above steps (Table 1). The drug curcumin 15 wt% and 20 wt% were desirably added to the acetalated-dextran and CMC phases, respectively from the stock solution in chloroform. This approach is supported by reports in the literature that hydrophobic drugs can be successfully emulsified or dispersed in the aqueous phase with the aid of surfactants or stabilizing agents particularly during double emulsion (W/O/W) based microsphere preparation, where the internal aqueous phase contains the drug for subsequent encapsulation in the polymeric shell.[55] The controlled single-phase system of acetalated-dextran (system S5) and Polylactic acid (PLA) (system S6) with drug curcumin and GOs were also fabricated using one-step emulsion techniques to compare the triggered release under the RF ablation. This followed the dissolution of curcumin (18 wt%) and 8 mg GO in acetalated-dextran (60 mg) based polymer solution prepared in DCM phase (450 μL) and PLA (45 mg) based solution prepared in the DCM phase (500 μL) for S5 and S6, respectively. The resulting oil phase (~500 μL) was poured into aqueous phase PVA (0.5 wt%) and mechanically stirred to achieve stable oil in water emulsion

Table 1 Compositions, particle size and effect on molecular weight after exposure to RF of different GO/curcumin loaded core–shell microspheres

System	Particle size (μm)	Location of graphene	Location of curcumin	GO content (%)	Encapsulation efficiency of curcumin (EE) %	Change in molecular weight of polymers[a] upon RF exposure (g mol^{-1})	
						Before	After
S1	258 ± 30	Shell	Shell	4.3	70 ± 1.5	36 904	32 495
S2	284 ± 12	Shell	Core	4.5	79 ± 1.0	36 904	34 313
S3	269 ± 24	Core	Shell	5.4	65 ± 0.5	36 904	36 292
S4	278 ± 27	Core	Core	5.5	82 ± 0.8	36 904	35 515
S5	226 ± 13	Uniformly dispersed	Uniformly dispersed	5.4	90 ± 1.3	36 904	35 702
S6	206 ± 11	Uniformly dispersed	Uniformly dispersed	5.3	93 ± 3.1	46 751	46 663

[a] Molecular weight of Ac-D polymer was determined for S1–S5 and Molecular weight of PLA polymer was determined for S6.

phases. The stirring (350 rpm) continued for 4 h at room temperature till the complete evaporation of solvent (DCM).[56–58] Another set of control microparticulate systems were also synthesized without the addition of GO. The fabricated microparticles were dried using lyophilizer and stored in a freezer for further characterization.

2.4. Characterizations

The prepared specimens were characterized by their structure, composition and drug release kinetics study. The morphological and layered structures were observed using field emission scanning electron microscopy (FESEM) (JEOL JSM-7800F Prime). The FESEM image analysis for particle size and layer thickness was done by ImageJ software. The layer compositions were confirmed using a micro-Raman spectrometer (GL127DW, U.K.) attached to an optical microscope of 20× magnifying lens. The samples and their cross-sections were irradiated with a laser of 785 nm, keeping the scanning range from 2000 to 100 cm^{-1}. The Raman spectra were collected following point-by-point mapping at different spots on the sample. The layer compositions were further verified from the confocal laser scanning microscope (CLSM Leica TCS SP8) where a blue dye poly(9,9-di-*n*-octylfluorenyl-2,7-diyl) was added to acetalated-dextran layer during the fabrication of microsphere. Additionally, the surface charges and ζ-potential of the microsphere were determined by using SurPass3 electrokinetic analyzer (Anton Paar GmbH, Graz, Austria) at pH 7.4. During the measurement, the pH was maintained by adding 0.05 M NaOH and 0.001 M KCl solutions. Powder X-ray diffraction (PXRD) analysis of microspheres was done in Ultima IV diffractometer (Rigaku) equipped with CuKα as an X-ray source. The measurements were taken in the 2θ range of 5–50° at a 4° min^{-1} scanning speed with a 0.02-degree step size. The surface chemical composition of the microspheres was determined using PHI 5000 Versa Probe III X-ray photoelectron spectrophotometer (Physical Electronics) having an Al Kα X-ray source and Ar ion gun. The high-resolution XPS spectra were deconvoluted using XPSPEAK4.1 software. A linear background was applied, and peaks were fitted using a mixed Gaussian–Lorentzian (GL) function. The software provides the chi-square (χ^2) value as an indicator of the goodness of fit. R^2 values are not directly reported by XPSPEAK4.1. Thermal stability of microspheres was determined by using thermogravimetric analysis (TGA, TA Q500, TA Instruments, USA) with the temperature scan from room temperature to 750 °C at 10 °C min^{-1} in N_2. Surface tensions and interfacial tensions of different phases were determined by Du Noüy ring method employing a tensiometer (K100, Krüss) (Table S1†). The Ac-D solution in chloroform exhibited surface tension of 20.188 mN m^{-1} and CMC solution in water produced a surface tension of 17.32 mN m^{-1}. The interfacial tension between different layers were determined by following literature reported eqn (1).[59,60]

$$\gamma_{IM} = \left(\sqrt{\gamma_I} - \sqrt{\gamma_M}\right)^2 \quad (1)$$

The drug encapsulation efficiency (EE) was determined by dissolving 5 mg of microspheres in 1 mL of DCM. The resulting mixture was centrifuged for 3 min at 3000 rpm to settle down the CMC, and the supernatant (drug-containing DCM phase) was collected. The solvent from the supernatant was evaporated by using vacuum. Then, 1 mL of ethanol was added to dissolve out the drug and the drug concentration were determined using UV-Visible-NIR Spectrophotometer (SHIMADZU UV-3600 I Plus) at 427 nm.[61] Before determining the corresponding λ_{max} for each concentration, a calibration curve of curcumin was constructed in ethanol solution. All experiments were performed in triplicates for each sample.

Swelling in the microparticles at predefined time intervals (used for the drug release study) was observed under an optical microscope. A change in size of particles due to the absorption of water in the presence of RF was determined by taking ~50 particles at different time intervals and calculating their swelling index with respect to the time. The swelling index provides an indication of microspheres' capacity to absorb water.[62]

Electric transport measurements of AcD/CMC and AcD-GO/CMC were determined by electrically contacting the samples (pellets of samples were prepared using hydraulic press) where R is the resistivity, L is the length of the conductor, A is the area of sample. The contact electrodes were made using commercial silver paste. Following applying two probes

between the outer current contacts with a B2912 source-measure unit, current voltage measurement was taken in 2 probe configuration using Probe station (form factor) in ambient condition using Keysight B2912B source meter.[63] Electrical conductivity (σ) was calculated using the equation mentioned below:

$$\sigma\left(\mathrm{S\,cm^{-1}}\right) = \frac{L(\mathrm{cm})}{A(\mathrm{cm^2})R(\mathrm{ohm})} \quad (2)$$

2.5. Drug release study

To investigate the drug release kinetics with and without the presence of RF stimulation, two set of experiments were conducted. Initially, the drug loaded microspheres (5 mg) were dispersed in a vial containing 1 mL of distilled water (0.035 mM) of pH 7.4 at 37 °C. At predetermined time intervals, 0.5 mL of the solution was collected from the vial and replaced with equal volumes of fresh distilled water of pH 7.4. The collected solution was lyophilized, and the curcumin concentrations were determined using UV–Visible-NIR Spectrophotometer at 427 nm by adding 0.5 mL of ethanol to it, since a calibration curve for curcumin was constructed in ethanol.

Further, these microspheres were exposed to RF fringing field generated from the parallel RF applicator, as shown in Fig. S2, Video S1.† The required RF field was amplified by setting up the frequencies from 140–160 MHz through an RF amplifier. The drug release kinetics study under RF was carried out by dispersing 5 mg of microspheres in distilled water (500 μL) of pH 7.4 in ceramic crucible by applying power ranging from 1–7 W to reach the desired temperatures, *i.e.*, 35–40 °C. The temperature in the system was measured using a FLIR camera (FLIR Systems Inc., A700). After settling down the particles at every time interval (5, 10, 20, 30, and 60 minutes), the supernatant (250 μL) containing the released drug were collected and crucible replenished with an equal amount of distilled water (0.035 mM) of pH 7.4. The concentration of each sample at different time intervals were determined using UV–Visible-NIR Spectrophotometer at 427 nm using the above-mentioned procedure and their cumulative release percentage was calculated with respect to time. Furthermore, initial morphological changes in the microspheres due to the RF ablation were observed using an optical microscope (Nikon Eclipse 80i) with magnification lenses of 10×.

Additionally, we have performed a set of control experiments to investigate the stability of the microsphere at room temperature 25 °C and at 40 °C. This was performed by dispersing two sets of microspheres (S1), 5 mg each in 1 mL of distilled water (pH 7.4, ionic strength: 0.001 M) at 25 °C as well as at 40 °C. At predetermined intervals, the sample was collected and monitored by UV–Visible-NIR spectrophotometer at 427 nm for 60 min using previously mentioned process. Besides, 5 mg of microspheres (S1) were dispersed in agarose gel (100 μL) to validate their stability in gel formulation, with and without RF exposure. The dispersed sample was transferred into the crucible pan and placed on the parallel plate applicator. The crucible having particles in gel exposed to RF following the same frequency used before. However, the particles in the gel required less than 1 W energy to reach the temperature 35–40 °C. The experiment continued for 1 h and the morphological changes were observed using an optical microscope.

2.6. Drug release kinetics and mathematical modelling

To elucidate the mechanism and kinetics of drug release from the prepared formulations (S1 and S4), the release data were fitted to various established mathematical models.[64] The cumulative percentage of drug released *versus* time data, obtained from the release studies, were subjected to linear regression analysis. The following kinetic models were employed:

• Zero-order model: the cumulative drug release (Q_t) was plotted against time (t). The zero-order release rate constant K_0 is determined from the slope of the plot.

$$Q_t = Q_0 + K_0 t \quad (3)$$

• First-order model: the logarithm of the percentage of drug remaining $\log(100 - Q_t)$ was plotted against time (t). The first-order release rate constant $K_1 = -(\text{slope}) \times 2.303$.

$$\log(100 - Q_t) = \log\left(100 - \frac{K_1 t}{2.303}\right) \quad (4)$$

• Higuchi model: the cumulative percentage of drug released (Q_t) was plotted against the square root of time ($t^{0.5}$). Higuchi rate constant K_H is determined from the from slope of the plot.

$$Q_t = K_H t^{0.5} \quad (5)$$

• Ritger–Peppas model

$$\frac{M_t}{M_\infty} = K_{rp} t^n \quad (6)$$

For each model, the coefficient of determination (R^2) was calculated to assess linearity and goodness of fit. Release exponent (n) indicating the release mechanism are derived from the slope. The rate constant $K_{rp} = 10^{\text{intercept}}$ and the physical significance of the best-fitting parameters was interpreted to infer the dominant release mechanisms.

2.6. Assessment of cytocompatibility of microspheres

Cell viability of the microsphere (S1) was assessed by MTT assay using HEK293 cells.[65] Briefly, HEK293 cells were cultured at 37 °C in a monolayer of DMEM with 10% (v/v) FBS in a humidified 5% CO_2 environment. Subsequently, healthy HEK293 cells were seeded in well plates (5×10^4 cells per well) with 200 μL of the media and allowed to grow overnight. Five concentrations of a freshly prepared suspension of system S1 microsphere were next added to the cells: 50 μg mL^{-1}, 250 μg mL^{-1}, 500 μg mL^{-1}, 750 μg mL^{-1}, and 1000 μg mL^{-1}.

Following a 24-hour cell incubation period, cell viability was assessed. After the completion of the exposure period, the medium was entirely withdrawn, and 200 μL of MTT reagent (0.25 mg mL^{-1}) was added after the cells had been cleaned once with PBS. After 3 h, the MTT reagent was removed and 100 μL of DMSO was added to dissolve formazan crystals formed due to interaction of cells with MTT reagent. Cells incubated with cell culture medium alone were used as positive control. Absorbance readings were measured at 570 nm and % cell viability was calculated as mentioned below:

$$\text{Cell viability}\,\% = \frac{\text{absorbance of treated cells}}{\text{absorbance of control cells}} \times 100 \qquad (7)$$

3. Results and discussion

3.1. Fabrication of Ac-D/CMC based core–shell microspheres

3.1.1. Methodology and process optimization. The drug carrier, core–shell microspheres composed of nanofibrillated CMC and acetalated-dextran (Ac-D) were fabricated by using emulsion techniques (Fig. 1). Prior to the fabrication of the microspheres, the precursor polymer, Ac-D soluble in organic solvent, was synthesized from dextran (water-soluble). The modification of dextran followed the protection of hydroxyl end groups with the acetal groups, making them more hydrophobic, increased solubility in organic solvents, and pH responsive.[66–68] The conjugation of the acetalated groups was confirmed from the proton NMR as shown in Fig. S1.† It was

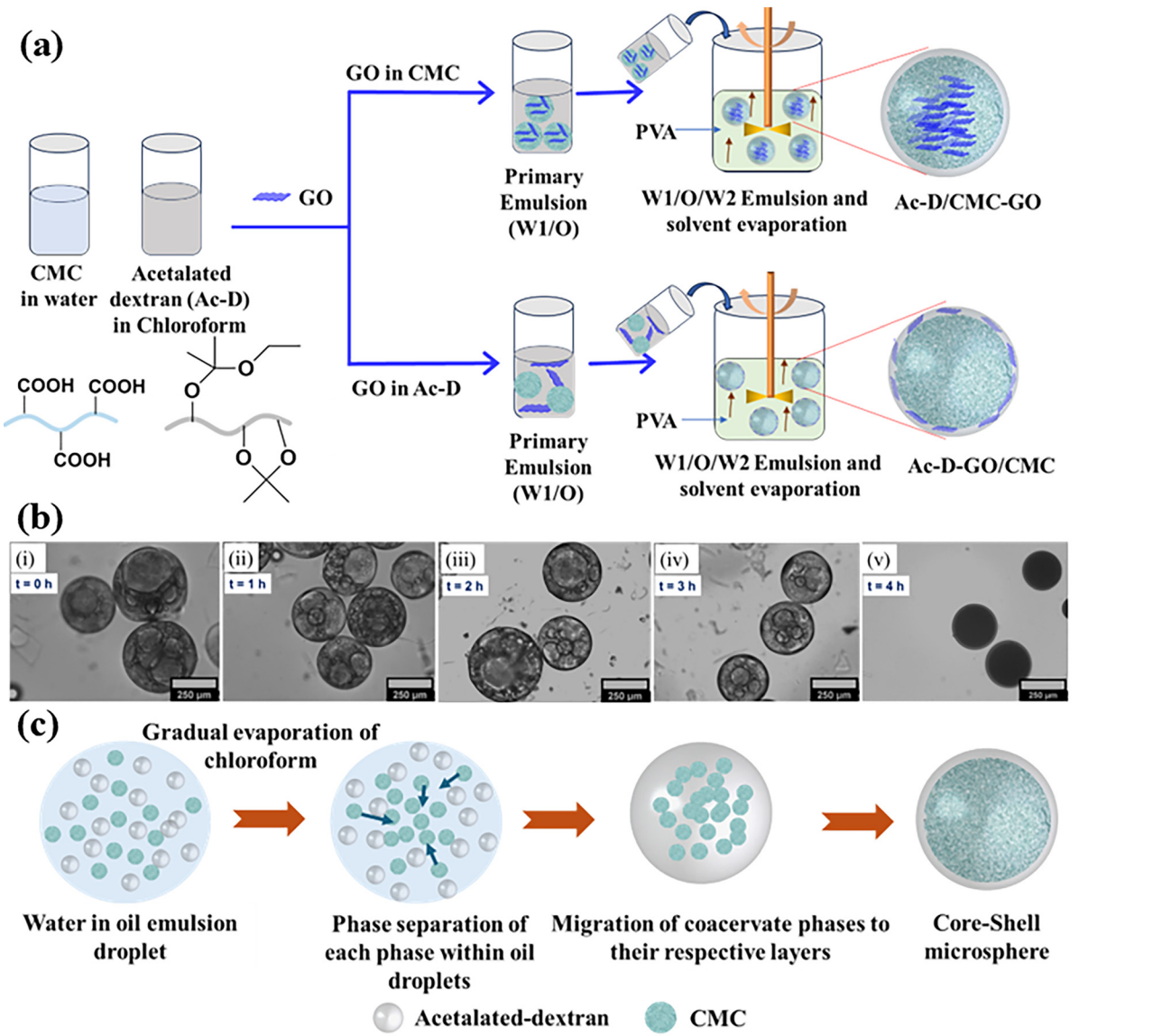

Fig. 1 (a) Schematic representation of formation of GO loaded core–shell microsphere systems, (b) optical images taken at different time intervals after the addition of primary emulsion to water containing PVA. (i) 0 h (ii) 1 h (iii) 2 h (iv) 3 h and (v) 4 h respectively, (c) schematic representation of plausible mechanism of the formation of core–shell microsphere system.

found that ~75% of total hydroxyl groups were converted into acetalated groups with the formation of cyclic to acyclic ratio of 1.58 : 1 in the modified polysaccharides.[69] Other precursors, CMCs were extracted from the pulp following an acid hydrolysis process in citric acid and confirmation of the formation of the nano-fibrillated CMCs was reported in our previous works.[36,70]

Fabrication of core–shell microsphere was carried out using double emulsion technique.[71,72] Porous and spongy nano CMC was used as a hydrophilic core material encapsulated by hydrophobic Ac-D layer to make the core–shell microspheres completely biodegradable, biocompatible, renewable and an ideal platform for capturing and releasing drugs (hydrophobic/hydrophilic) in controlled rate at desired places. The preparation of emulsion phase1 (Water (W1) in Oil (O)) was carried out by pouring the dissolved CMCs in NaOH/urea solution in oil phase (O) containing the Ac-D in DCM (Fig. 1). The mixture was further probe sonicated to get a homogenous emulsion phase. The resulting emulsion phase (W1/O) was transferred into a PVA solution (W2) to get the stabilized emulsion droplets. The slow evaporation/diffusion of solvent (Chloroform) from Ac-D in the first emulsion phase into the W2 resulted in the shell hardening, thereby entrapping the CMCs as core in the microsphere.

3.1.2. Mechanism of core–shell formation. The mechanism of formation of core–shell microspheres was further assessed following *in situ* observation of emulsion droplets using an optical microscope at different time intervals after the addition of primary emulsion to the phase containing PVA (Fig. 1b). The phase separation followed by migration of coacervate phases towards each other was observed in the optical images, as can be seen from Fig. 1b(i–iv). Images were captured over time starting from 0 h to 4 h at different intervals showing the formation of multiple small droplets within a large droplet and their subsequent coalescence towards their respective phases. The formation mechanism of core–shell microspheres was further verified by using the spreading coefficient theory.[71,72] The solvent evaporation from double emulsion droplets can result in three states, namely, partial wetting, complete wetting, and dewetting. The formation of core–shell morphology is a result of a complete wetting phenomenon. This can be estimated from the interfacial tensions (γ) between immiscible liquid droplets, designated as inner phase (I: CMC), middle phase (M: Ac-D) and outer phase (O: water) (Table S2†). From these values, spreading coefficient (S) of each phase can be calculated (Table S2†). For example, a general equation for calculating the spreading coefficient of middle layer, S_M is given below in eqn (8).[60]

$$S_M = \gamma_{IO}\ (\gamma_{IM} + \gamma_{MO}) \quad (8)$$

From the calculation, we have obtained $S_M < 0$, $S_I > 0$ and $S_O < 0$, thus meeting the criteria for complete wetting. This further indicated that the hydrophilic inner layer (CMC) was being completely engulfed by the hydrophobic middle layer (Ac-D), as desired. Additionally, higher volume ratio between chloroform and water during the formation of primary emulsion can further drive the successful entrapment of CMC in Ac-D layer.[72] It is well documented that during the formation of kinetically entrapped core–shell structure, the component with higher volume typically forms the shell by enclosing the lower volume component as core.[73] Finally, gradual evaporation of chloroform from the middle layer solidified the shell to produce core–shell microspheres (Fig. 1c).

This investigation aims to study the *in vitro* release behavior of the drug under electromagnetic fields in the RF range. To make the above particulate systems RF responsive, we incorporated ultrathin graphene oxide (GO) into microsphere following the same procedure as stated above. Graphene oxide is a two-dimensional carbonaceous ultrathin (thickness is in nm) material with excellent thermal conductivity and can generate heat waves when exposed to RF fields.[74,75] We hypothesized that the RF heating would lead to microspheres' swelling and pore formation, eventually accelerating the release of entrapped drugs from the microspheres into the surrounding system through disintegration. Additionally, ultrathin GO has high surface area, biocompatibility, and inherent surface functionalities, which facilitated their better dispersion in the matrix along with improved drug loading. These attributes make GO an ideal RF responsive tar to be incorporated in drug carriers.[76,77] Before the addition of the GOs, we modified the GOs using Hummer's method[54] and the comparative characteristic properties, such as structure and morphology, were depicted in Fig. S3.† The incorporation of GOs in different layers as core (Ac-D/CMC-GO) and shell (Ac-D-GO/CMC) materials were attributed to the varying responsiveness of the embedded GOs towards the RF field (Fig. 1a, Table 2). In order to determine its RF permittivity, electrical conductivity of the microsphere was evaluated. According to multiple studies, GO exhibits electrical conductivity between 10^{-5} and 10^{-7} (S cm^{-1}),[78,79] while Ac-D/CMC and Ac-D-GO/CMC displayed 2.89 $\times$ 10^{-12} and 1.51 $\times$ 10^{-8} S cm^{-1}, respectively (Table S3†). This implies that higher electrical conductivity of Ac-D-GO/CMC may enable them to readily conduct RF waves, whereas Ac-D/CMC with lower electrical conductivity would severely impede RF wave propagation, hence acting as an insulator.

3.2. Determination of layer compositions

The formation of the core–shell microsphere, layer compositions, and the distribution of the encapsulated materials were evaluated using characterization techniques such as FESEM, Raman, PXRD, and XPS. The FESEM analysis revealed that both types of microspheres (size: 280 ± 20.5 μm) exhibited a sphere-shaped morphology having a porous core (Fig. 2). A clear distinction between the spheres

Table 2 Composition, particle size, and location of GO

System	Particle size	Location of GO
Ac-D/CMC-GO	237 ± 47 μm	Core
Ac-D-GO/CMC	262 ± 51 μm	Shell

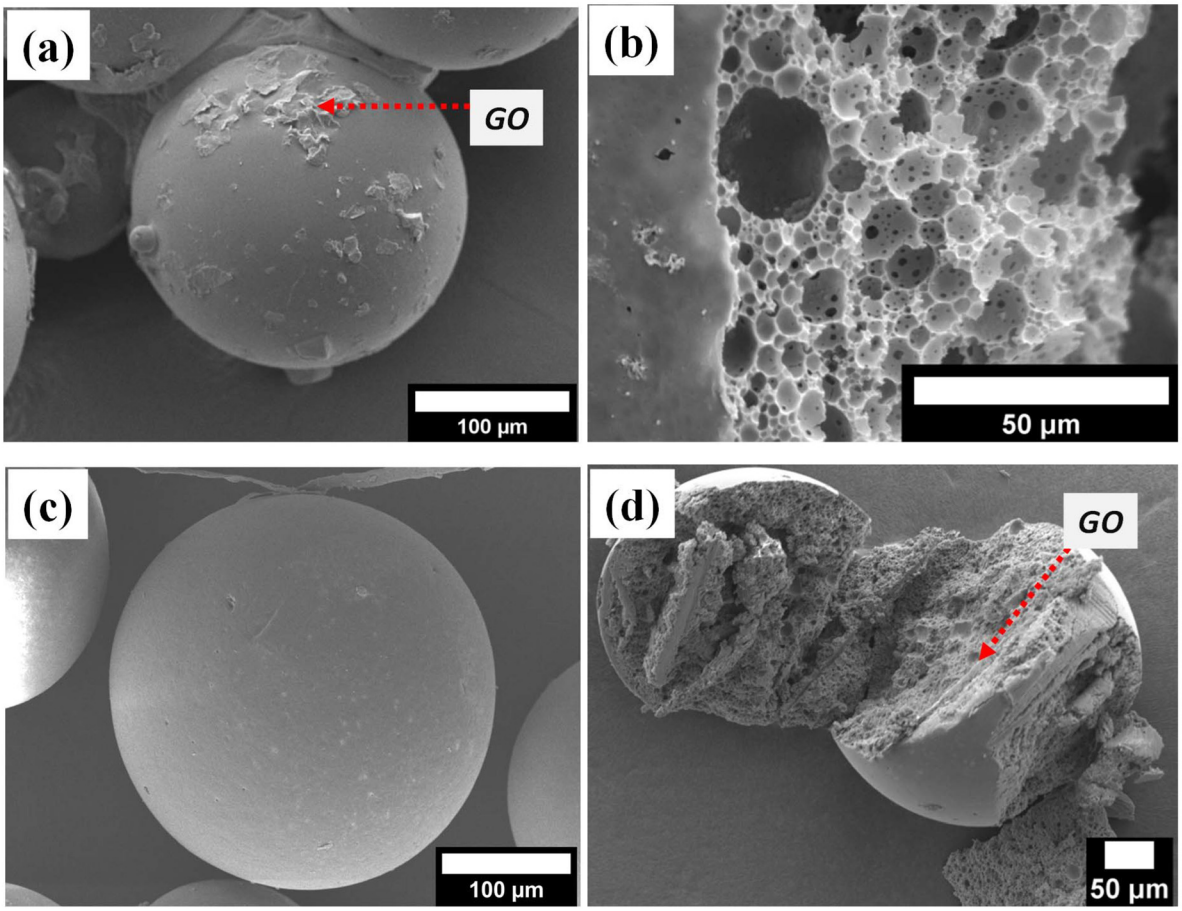

Fig. 2 FESEM images of GO loaded core–shell microsphere systems. (a) and (b) for FESEM and cross-sectional FESEM images of Ac-D-GO/CMC (GO in the shell), (c) and (d) for FESEM and cross-sectional FESEM images of Ac-D/CMC-GO (GO in the core) respectively.

having GO in the core and the shell was evident from the FESEM analysis. Ac-D-GO/CMC (GO in the shell) microsphere (Fig. 2a), exhibited wrinkled sheets on their outer surface distributed throughout the surface of the particles, whereas Ac-D/CMC-GO (having GO in the core) produced smooth surfaces indicating complete entrapment of GOs in the core (Fig. 2c). This can also be seen from the cross-sectional images of the microsphere (Fig. 2d) where the GOs were embedded into the inner layers of the porous matrix of the CMCs. TGA analysis was carried out to assess the amount of entrapped GOs. The results showed that around 4.4 wt% GO (*i.e.*, encapsulation efficiency of GO: 55%) was loaded in the case of Ac-D-GO/CMC, whereas it was 5.6 wt% (*i.e.*, encapsulation efficiency of GO: ~70%) for Ac-D/CMC-GO systems. This difference could be due to the reduced thickness of the solid shell layer in comparison to the porous core layer. Moreover, the layer compositions of microspheres (Ac-D/CMC) were further verified by caging a blue light emitting polymeric dye poly(9,9-di-*n*-octylfluorenyl-2,7-diyl) in the shell layer (Ac-D), during the fabrication process. The entrapped polymeric dye can be seen under the CLSM with intense blue colors in the shell layer only (Fig. S4†), indicating the formation of well phase separated core–shell microspheres during the solvent evaporation emulsion technique.

The layer composition and distribution of GO in the microspheres were also analyzed using Raman spectroscopy, with point-by-point mapping of each layer and the results were displayed in Fig. 3 and Fig. S5.† For comparison, Fig. S5† shows the Raman spectra for Ac-D/CMC micropshere without GO. A characteristic peak at 1101 cm^{-1}, corresponding to β-(1,4)-glycosidic linkage,[80] indicated that the core primarily consisted of CMC. Peaks in the 1440–1470 cm^{-1} range for $–CH_2$ stretching and at 977 cm^{-1} for –C–O–H bending confirmed that the shell was made of Ac-D.[35] The $–CH_2$ stretching and –C–O–H bending vibrations at ~970 cm^{-1} were found in both the core and shell, likely due to Ac-D adsorption onto porous CMC surfaces during solvent evaporation. No CMC-related peaks were observed in the shell, further confirming no CMC migration to that layer. The spectra in Fig. 3a and d for GO loaded micropshere having peaks at 1592 and 1599 cm^{-1} for GO in the core and shell respectively, corresponded to the G-band of GO, slightly shifted from the neat spectrum (1586 cm^{-1}), indicating its interaction with Ac-D. In Fig. 3d, the Ac-D/CMC-GO micro-

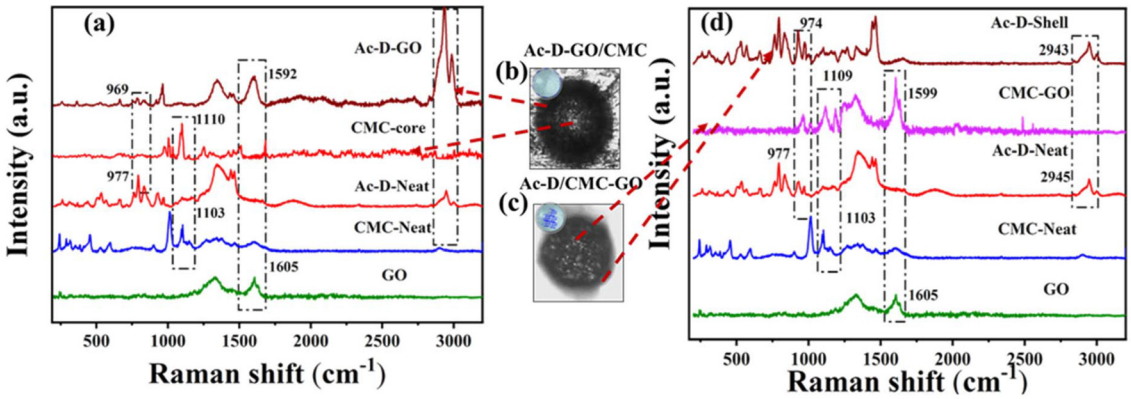

Fig. 3 Raman spectra of (a) Ac-D-GO/CMC (GO in shell) and (d) Ac-D/CMC-GO (GO in core) and (b and c) show their corresponding optical images taken during the point-by-point mapping.

spheres show no dextran peaks in the core, but a peak at 1599 cm^{-1} confirmed the presence of GO in the core. Overall, Raman spectra evidently affirmed the layer compositions indicating the formation of core–shell microsphere and the uniform distribution of GO in the respective layers.

PXRD analysis was performed on both Ac-D-GO/CMC and Ac-D/CMC-GO samples and compared with pristine GO, Ac-D, and CMC to confirm the presence of GO at desirable locations (Fig. 4). Due to overlapping diffraction patterns, XRD could not clearly differentiate between the core and shell structures. Ac-D produced a broad signal (15–28°),[81] masking the characteristic CMC peak at ~22°. Nevertheless, the PXRD pattern of the Ac-D-GO/CMC sample displayed a strong diffraction peak at ~10.3°, corresponding to the (001) plane of GO.[82] A weaker ~10.3° peak in the Ac-D/CMC-GO sample indicated the GO's presence in the core, as the X-ray penetration was limited in the core region. This confirmed the successful fabrication of core–shell microspheres, with GO positioned either in the core or shell as intended.

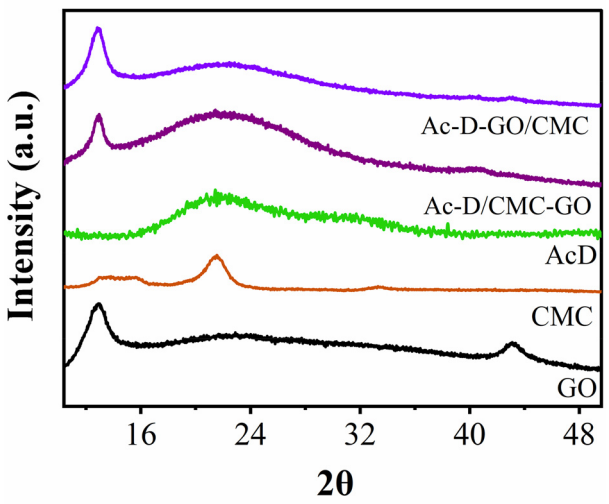

Fig. 4 PXRD analysis for GO incorporated core–shell microspheres.

3.3 Determination of surface functionalities

XPS was performed on both microspheres to further analyze the surface elemental compositions and their tentative locations. XPS is ideal for indirectly characterizing core–shell structures due to its excellent surface sensitivity (depth of penetration: 5–10 nm). The data was compared with pristine Ac-D and GO, excluding CMC, as it was primarily confined to the core. Pure CMC typically shows three distinct peaks in the C 1s spectrum at binding energies of approximately 284.8 eV, 286.3 eV, and 287.8 eV, corresponding to C–C/C═C, C–O, and C–O–C bonds, respectively (Fig. 5a). In all samples, two main peaks were observed at 284.8 and 285.9 eV, attributed to C–H/C–C and C–O bonds arising from Ac-D. In the Ac-D-GO/CMC microspheres (with GO in the shell), an additional peak around 287 eV, corresponding to the C═O bond in GO, was detected, confirming GO's presence in the shell. The broader C 1s spectra in Ac-D-GO/CMC as compared to the pristine Ac-D and Ac-D/CMC-GO, may originate due to the exposure of graphitic sp^2 C on the surface, causing the peak to merge with the main spectrum, further indicating GO's predominance in the shell. In contrast, no such C═O peak was detected when GO was located in the core of Ac-D/CMC-GO. This finding was further supported by O 1s spectra analysis (Fig. 5b). A predominant peak at ~530.1 eV was observed in all samples, corresponding to C–OH bonds in Ac-D. Pristine GO exhibited peaks at 530.2 eV (C–OH) and 533.4 eV (C═O). In Ac-D-GO/CMC, an additional peak at ~533.2 eV, corresponding to C–O–C/C–OH from GO, confirmed its presence in the shell. No such peak was detected in Ac-D/CMC-GO, where GO was confined to the core. These results confirmed the successful formation of core–shell microspheres with GO in the shell for Ac-D-GO/CMC and in the core for Ac-D/CMC-GO particles. For comparison, the χ^2 values for the C 1s spectra of AcD, GO, AcD/CMC-GO, and AcD-GO/CMC were found to be 0.62, 0.73, 0.82, and 0.78, respectively. Similarly, for the O 1s spectra, the corresponding χ^2 values were 0.73, 0.95, 0.79, and 0.86, respectively. These values (<1) confirm the overall consistency and robustness of the peak fitting across all samples.

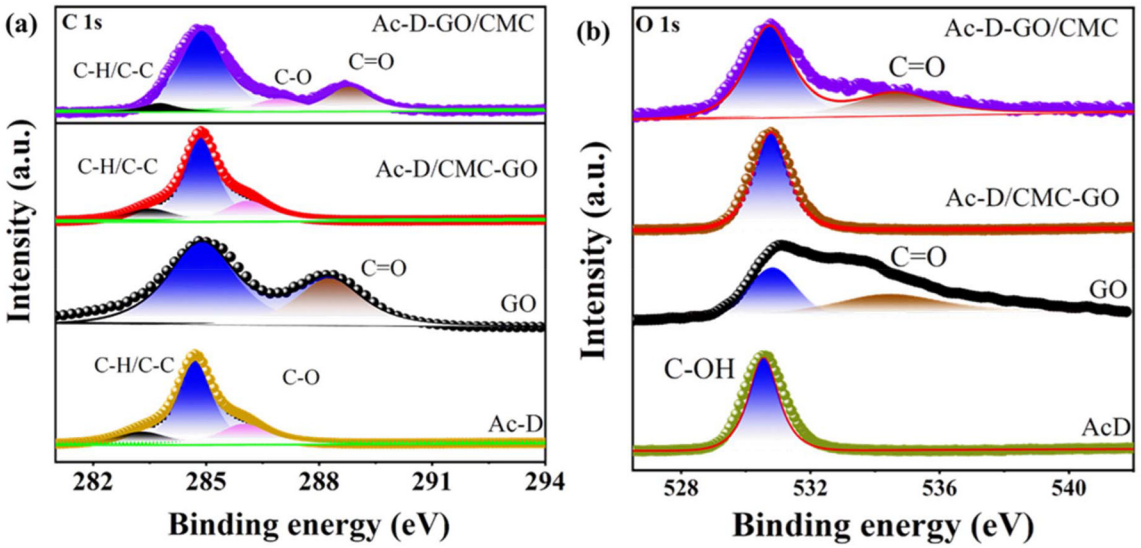

Fig. 5 XPS analysis of synthesized microspheres (a) comparative C 1s spectra of neat Ac-D, neat GO, Ac-D/CMC-GO and Ac-D-GO/CMC, (b) comparative O 1s spectra between neat Ac-D, neat GO, Ac-D/CMC-GO and Ac-D-GO/CMC.

Surface charge is an important characteristic property of microsphere made from materials such as Ac-D and CMC with rich hydroxyl groups. The surface charges of Ac-D, Ac-D/CMC-GO and Ac-D-GO/CMC were determined by measuring their surface ζ-potentials at pH 7.4 (Fig. S6†). Ac-D based microsphere without GO were taken as a control, showing a ζ-potential of −30 mV, due to electronegative acetal groups contributing to a negative charge, in line with the previously reported literature.[57] Nevertheless, Ac-D-GO/CMC having GO in the shell exhibited significantly higher negative surface charges (−90 mV) in comparison to Ac-D/CMC-GO having GO in the core (−55 mV). The electronegative functional groups (–OH, –COOH *etc.*) that were created on the surface of the graphitic lattice during the oxidation process were assumed to be responsible for the enhancement of the negative zeta potential values, especially when GO was in the shell.[83,84] Conversely, a minimal change of surface charge was evident when GO was in the core.

3.4. Encapsulation of drug in the microspheres

To investigate the RF sensitivity of the microspheres, we designed and created five sets of GO-containing microspheres encapsulated with a model drug, curcumin (CUR) so that the release of curcumin triggered by RF can be assessed. The locations of GO and CUR were illustrated in Table 1 and Fig. S7.† The morphological micrographs of the microparticles and their cross-sectional images were shown in Fig. 6. This was purposefully done to evaluate the role of GO location in RF conductance and drug release. In the first two systems (S1 and S2), GO was located in the shell, whereas the CUR was entrapped either in shell or in core. However, the second sets (S3 and S4) had GO in the core with CUR either in shell or in core. Furthermore, in order to investigate the role of core–shell architectures and the type of matrix in triggering drug release as shown by the Ac-D-GO/CMC and Ac-D/CMC-GO microspheres, two additional sets of microspheres were further created. System S5 was composed of AC-D, GO and CUR without any core shell architecture and S6 consisted of a hydrophobic biodegradable polymer such as PLA (as matrix) along with GO and CUR, uniformly distributed throughout the matrix. PLA was selected as a hydrophobic matrix as an alternative to the hydrophilic porous spongy core such as CMC, to understand the role of matrix in dissipating RF and triggering the drug release. Presumably, due to the distribution of GO throughout the bulk of microparticles, the surface of S5 and S6 particles appeared to be smooth as shown in Fig. 6e and f.

CLSM analysis (Fig. S8†) further confirmed the CUR's localization, with CUR remaining in the shell when encapsulated there, however, uniformly distributed throughout the microspheres when entrapped in the core, likely due to CUR's hydrophobicity and its affinity for the hydrophobic shell, *i.e.*, Ac-D layer.

Before performing an *in vitro* release study, the encapsulation efficiencies of CUR for S1–S6 were evaluated and tabulated in Table 1. It was found that the encapsulation efficiencies of CUR for S1 (~68%) and S3 (~65%) were slightly lower than that for S2 (~79%) and S4 (~82%), probably due to the reduced thickness of the Ac-D layer favoring less drug-polymer interaction and also porous CMC core capable of trapping higher amount of CUR. However, compactness and hydrophobicity of S5 (~90%) and S6 (~93%) promoted enhanced encapsulation efficiency.

3.5. Radiofrequency (RF) triggered drug release

3.5.1. RF-triggered drug release profiles. Release profile of curcumin with or without RF exposure was monitored to examine the efficacy of various microsphere systems (Table 1)

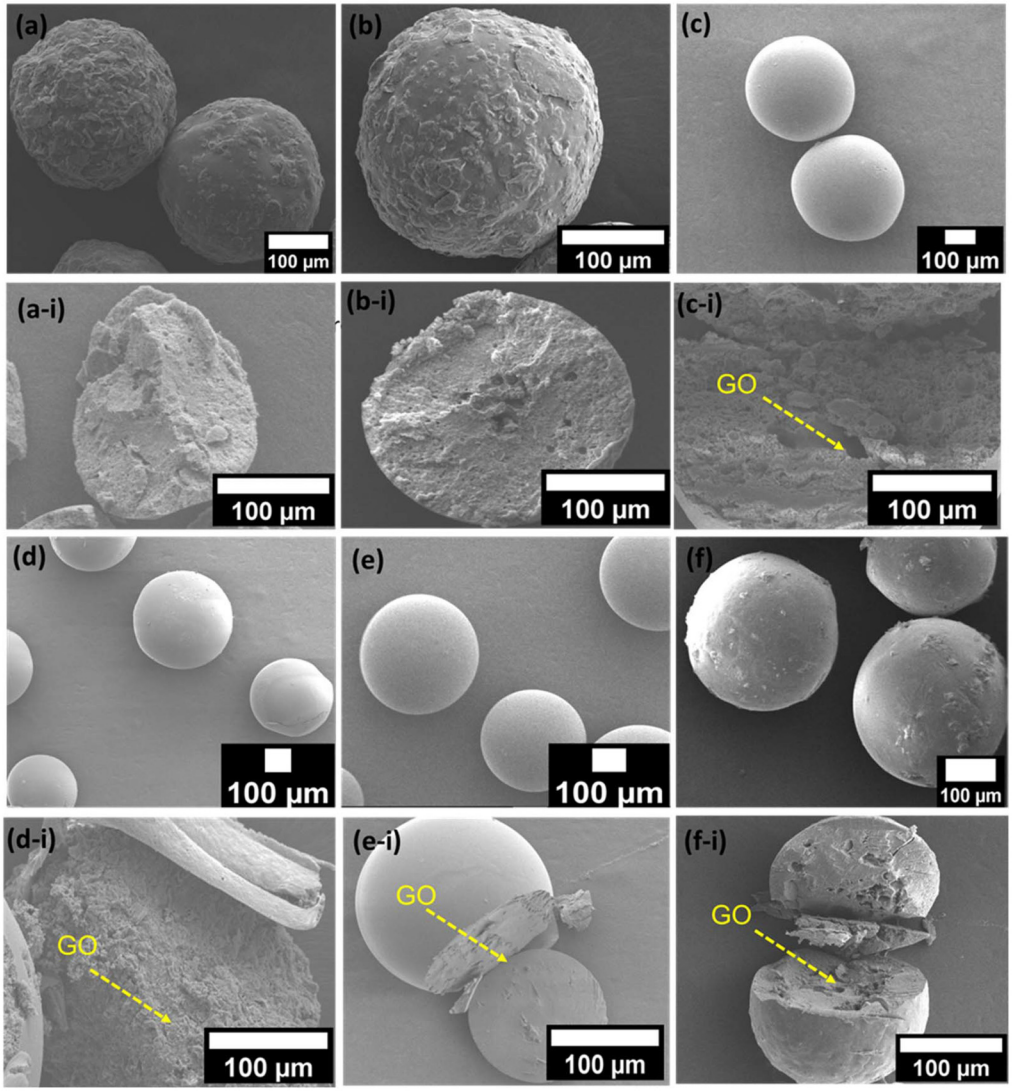

Fig. 6 FESEM images of different GO/curcumin systems loaded with their cross sections. S1(a), S2(b), S3(c), S4(d), S5(e), S6((f)) and (a-i, b-i, c-i, d-i, e-i, and f-i, represent their corresponding cross-sectional images).

under external stimulus (Fig. 7). Without an external stimulus (RF) the drug release from the various systems was minimal (<2% within 60 minutes) owing to the stability of acetalated-dextran layer under physiological pH. However, when these systems were irradiated with a 5 W, 142 MHz radiofrequency (optimized condition), a rapid drug release (>60% drug release within 10 min for S1) was noticed, clearly indicating the role of RF in triggering the drug release. The drug release profile was found to be in the following order: S1 > S2 > S4 > S3 > S5 > S6, *i.e.*, a progressive reduction of cumulative drug release was observed from S1 to S6, exhibiting the importance of the location of GO and drug along with matrix type in accelerating the drug diffusion. In case of S1 and S2 having GO in the shell exhibited faster drug release under RF exposure as compared to the S3 and S4 systems containing GO in the core. This could be attributed to the increased absorption and conduction of waves due to the easy accessibility and availability of GO in the shell, though GO content in the core was slightly higher (1% more).[82] It is noteworthy that the S4 system having drug and GO both in the core, sped up the drug release as compared to the S3 system having GO in core and drug in shell. This indicated an enhanced interaction between drug and GO upon exposure to RF, when they were in the same compartment, thus accelerating the drug release. Upon exposure to RF, the swollen hydrophilic cellulosic core may undergo oscillation, hence rupturing the core and triggering the drug release from core. Nevertheless, GO loaded Ac-D based (S5) and PLA-based monophasic microparticles (S6) without having any core shell morphology showed only 50% and <8% drug release within 60 minutes, respectively under the same conditions as stated above (Fig. 8). Besides, affinity of hydrophobic drug towards relatively hydrophobic PLA matrix may further slower the drug release. In addition to this, we performed a set of control experiments to investigate the stability of the microsphere at

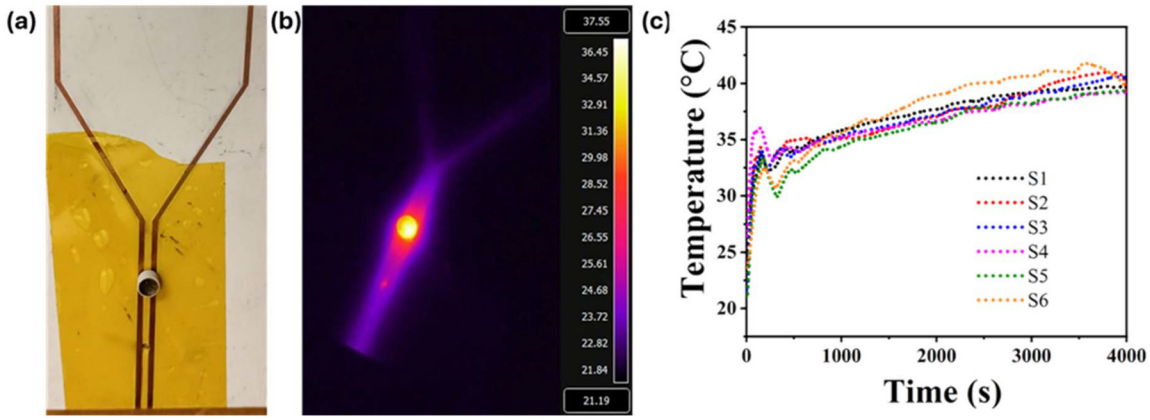

Fig. 7 (a) Applicator used for RF ablation (b) thermal imaging using IR camera during RF heating (c) RF heating response of samples.

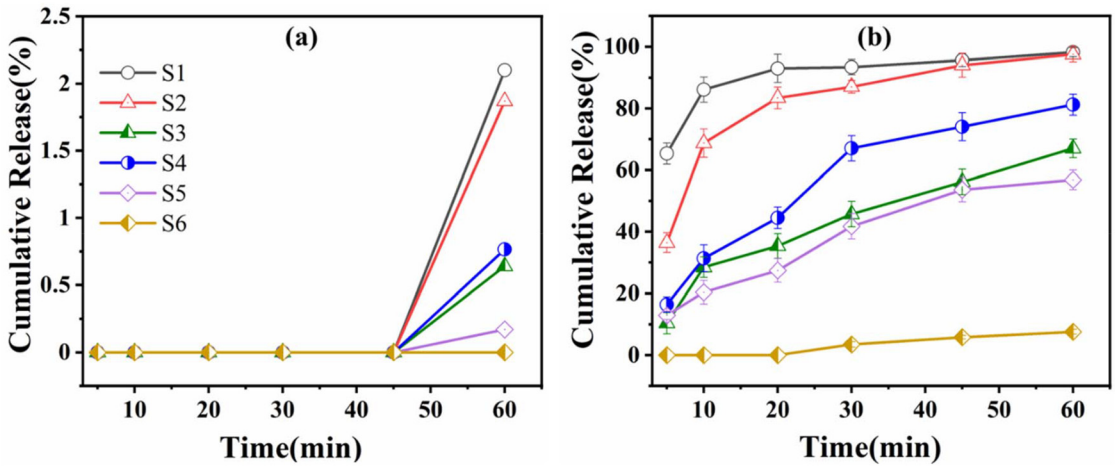

Fig. 8 The drug release profile from the core–shell microspheres (a) S1–S6 without and with (b) RF exposure.

room temperature 25 °C and 40 °C. The results demonstrated that the microsphere remained stable under both conditions, with no drug release observed at 25 °C and only 2.7% release at 40 °C (Fig. S9†). These findings further confirm that RF stimulation is the primary factor contributing to the substantial drug release within this time span.

3.5.2. Drug release mechanism. To elucidate the underlying mechanism governing drug release, cumulative release data were fitted to established kinetic models, namely first-order, Higuchi, and Ritger–Peppas models (Fig. S10†). Two representative microsphere systems were investigated: S1, where curcumin and GO are co-localized in the Ac-D shell, and S4, where both components are embedded within the CMC core. These spatial configurations were selected to evaluate the influence of drug and GO location on release kinetics and RF responsiveness. Quantitative drug release studies demonstrated clear differences between S1 and S4 as discussed in previous section (3.5.1, Fig. 8). S1 exhibited a pronounced burst release (~65% in 5 minutes, ~98% by 60 minutes), whereas S4 showed a more gradual release (~16% in 5 minutes, ~81% by 60 minutes). The rapid release in S1 is primarily attributed to the shell localized positioning of both the drug and GO. In this arrangement GO, being the primary RF-responsive agent, is in direct contact with the applied RF field, enabling efficient energy absorption and localized heating through dielectric loss and eddy current mechanisms.[85] This interaction facilitates rapid loosening of the Ac-D matrix, enhances drug diffusion, and accelerates release. Conversely, in S4, both drug and GO are embedded deep within the CMC core. As a result, RF penetration and energy transfer to GO are delayed, causing a slower initial response. The hydrophilic CMC matrix also needs to swell before effective diffusion can occur, contributing to the lag phase in release.[36]

To further understand the diffusion of the drug from the polymeric microspheres under RF heating, we have used different kinetic models such as zero order, first-order, Higuchi, and Ritger–Peppas models for S1 and S4 systems only (Fig. S10, Table S4†), as mentioned above. The analysis confirmed distinct mechanistic pathways influenced by GO location and matrix properties. For S1, where curcumin and

GO were encapsulated in a hydrophobic Ac-D shell, the poor fits of the first-order (R^2 = 0.89) and Higuchi (R^2 = 0.71) models indicate that the release did not purely follow concentration-driven or diffusion-limited kinetics. However, good fitting with the Ritger–Peppas model in two stages revealed a biphasic mechanism. The similar burst release is also seen at the first stage, well fitted by Ritger–Peppas model, as reported by others:[13,14] Stage 1 (0–20 min) showed Fickian diffusion (R^2 = 0.97, n < 0.25), while stage 2 (20–60 min) exhibited a slower and restricted release (R^2 = 0.98, n < 0.10), probably due to drug stabilization by Ac-D matrix and potential GO–drug interactions as well, since majority of the drug had already diffused out during the initial phase (stage 1). In contrast, S4, containing curcumin and GO in a hydrophilic CMC matrix, exhibited strong fits across First-order (R^2 = 0.97), and Higuchi (R^2 = 0.96) models, indicating sustained, consistent release. The Ritger–Peppas model (R^2 = 0.97, n = 0.64) too showed good fit for S4 system and confirmed anomalous transport involving both diffusion and polymer matrix swelling. These model-derived insights strongly correlate with our experimental observations (Fig. 9) and hypothesized mechanism, *i.e.*, shell-localized GO systems (S1) enabled rapid RF response and drug release due to high exposure and minimal diffusion barriers, whereas core-localized GO systems (S4) exhibited sustained release governed by diffusion and matrix swelling.

3.5.3. Morphological analysis of microspheres post RF exposure. Post RF exposure, morphological analysis was performed on these systems using FESEM (Fig. 9) and optical images (Fig. S11†). The results indicated that the microspheres could not retain their structural integrity after exposure to the RF waves leading to their rupture and rapid release of the entrapped drug from its matrix, especially for S1 and S2 systems. It can also be pointed out that the protective shells were not solely peeled off or degraded, rather the whole microspheres got disintegrated, probably due to the bursting out of the swollen microspheres (discussed later). Nevertheless, in the case of S5, the surface of the spheres was observed to form cracks leading to minimal drug release within 60 minutes of RF exposure. Interestingly, no such crack or disintegration was noticed for S6 comprised of PLA (Fig. 9f and S11f†). Moreover, the spherical structure of the S6 particles remained intact with minute pore formation seen on their surface, thereby restricting the burst release of curcumin (<8%). To validate the role of GO in RF responsiveness, microspheres devoid of GO were also fabricated and irradiated with RF. As expected, no change of morphology or shape was evident (data not shown). Additionally, stability study using microspheres from S1 system incorporated into a gel formulation was performed to simulate conditions relevant to topical drug delivery. The formulation was evaluated both with and without RF stimulation. Under ambient conditions without RF, the microspheres remained structurally stable within the gel, showing no signs of degradation or morphological changes over time. In contrast, upon RF exposure, the microspheres exhibited structural (physical) rupture, as confirmed through optical microscopy (Fig. S12†). These observations support the conclusion that the RF-responsive microspheres maintain integrity under normal conditions but respond effectively to external RF triggers, validating their potential for topical drug delivery applications with controlled, on-demand release.

To rule out the chemical change of Ac-D (shell) upon exposure to RF, GPC (Table 1) and NMR analysis of the disintegrated microspheres were performed. No change of characteristic peaks corresponding to Ac-D was noticed in the NMR

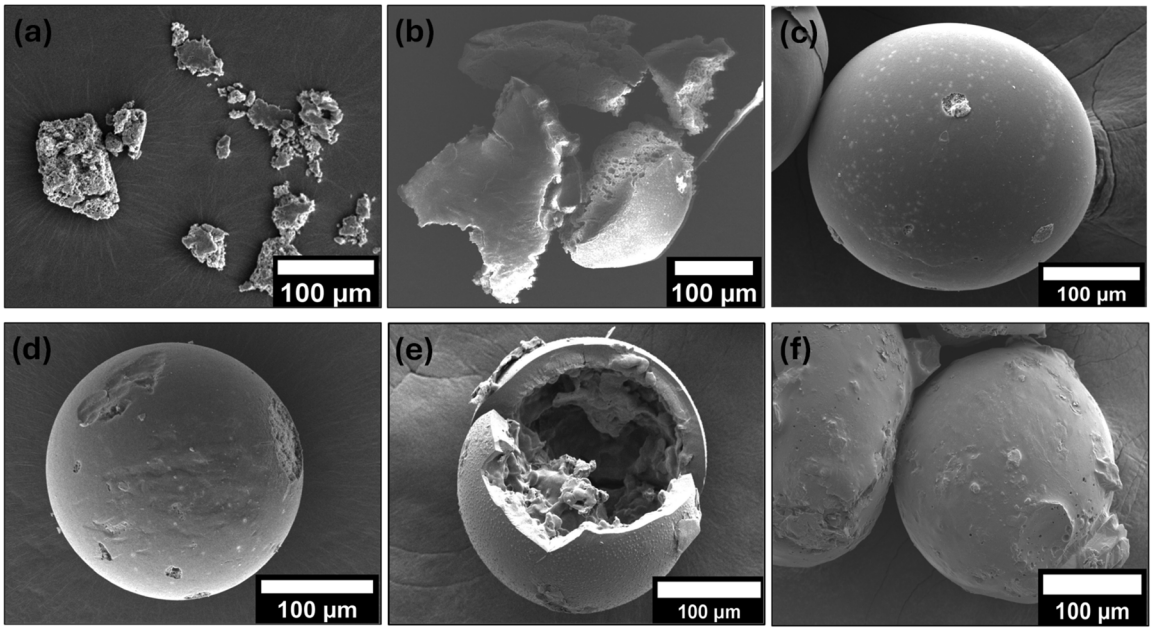

Fig. 9 Representative FESEM micrographs for (a-S1, b-S2, c-S3, d-S4, e-S5, f-S6) after RF treatment during drug release profile study.

spectrum and negligible change in the molecular weight was observed in the samples after RF exposure (Fig. S13†), indicating no significant change in chemical structure of the polymeric materials occurred upon RF exposure.

To establish the effect of RF in rupturing the microsphere and subsequent drug release, change in temperature of the medium and swelling index (Fig. S14†) of these particles were also recorded. As shown in Fig. 7c, a maximum increment in temperature from 25 °C to 41 °C was observed for S6 samples. We have applied the same range of RF power to all systems to maintain temperature but for the S6 we observed slightly higher temperature due to a good, percolated network of graphene in PLA matrix. This could be due to the presence of relatively hydrophobic PLA matrix, which would tend to bind minimum water on its surface and bulk as well (exhibiting minimum swelling index, Fig. S14†), thus generating maximum energy dissipated as heat arising from high dielectric loss upon RF treatment.[86] This could further be facilitated by their densely packed matrix comprised of higher molecular weight polylactide chains (M_n of PLA: 46 571 g mol^{-1}) in comparison to Ac-D (M_n of Ac-D: 36 904 g mol^{-1}). Nonetheless, the temperature change was insufficient to disintegrate the PLA due to its higher thermal stability (T_m (melting temperature): 150 °C, T_g (glass transition temperature): 60 °C and T_d (thermal decomposition temperature): 290–380 °C), as reported in literatures.[87,88] For all the other systems (S1–S5), the maximum-recorded temperature was only 40 °C, measured within the stipulated period. The minimal temperature increment ruled out the significant impact of temperature on their ruptures, since all the thermal transitions for the employed polymers were much above 40 °C (T_m and T_d for Ac-D are 170 °C and 290 °C, respectively,[88] whereas T_d of CMC: 266 °C[89]). Moreover, a mild temperature increment further implied that the RF assisted heating hardly contributed to the rupture of susceptible chemical bonds in the microspheres, since around 90 °C was required for breaking the acetal bonds in Ac-D under neutral pH using water as solvent.[90] Desirably, the mild heat generated during RF exposure should not harm the healthy tissues/cells, making it an attractive tool for triggered' drug release *in vivo*. Moreover, to determine the potential loss of GO after RF exposure, we have also conducted control experiments by subjecting synthesized microspheres (Ac-D/CMC-GO and Ac-D-GO/CMC) to RF. Subsequently, TGA analysis was performed on exposed particles (Fig. S15†) to show marginal loss in GO content following RF exposure. This further highlighted the stability of GO within the microspheres and eliminated the possibility of leaching out of GO due to RF exposure, which can be considered as an advantage for drug delivery applications.

Besides, swelling index of the systems (S1–S6) were measured in water to determine whether the core shell microspheres underwent considerable swelling upon their exposure to RF or not. The results displayed in Fig. S14b† clearly demonstrate that a significant swelling (~60–70%) was noticed upon exposure to RF of 20 minutes for all the core–shell microspheres (S1–S4), probably due to the presence of hydrophilic porous cellulosic core. However, marginal swelling (~10%) and almost no swelling (<5%) were observed for S5 and S6 samples (Fig. S14b†), respectively, further correlating with their sluggish drug release profiles and enhanced heat accumulation for S6, as mentioned above.

3.5.4. Mechanistic insights into RF-triggered release. Considering all the findings described above, it can be suggested that upon absorbing the RF waves, GO facilitated the spreading of the energy throughout the matrix, especially when GO was in the shell of the spheres. Specifically, the localization of GO and its interaction with RF waves (in the core or shell) play a pivotal role in RF-triggered drug release and the overall responsiveness of the microspheres. When located in the shell, GO was directly exposed to RF waves, facilitating the effective conversion of RF energy into localized heating, thus accelerating the drug diffusion. Conversely, GO in the core may undergo partial shielding, thus minimizing the direct RF interaction, resulting in an extended-release profile. Thus, systems with GO in shell (S1 and S2) exhibited faster drug release due to enhanced RF wave absorption and energy conduction, whereas systems with GO in the core (S3 and S4) displayed slower release profiles due to limited penetration of electromagnetic wave. This enhanced interaction led to faster energy transfer and rapid disintegration of the microspheres. Additionally, the force that radiofrequency (RF) exerted on these negatively charged polymeric systems may cause dielectric polarization, which in turn may account for dielectric loss through energy dissipation as heat.[91] Dielectric loss is key to RF-induced heating, depending on GO localization. The shell-localized GO may maximize the RF absorption and energy dissipation, thus accelerating the drug release, while core-localized GO was shielded by the polymer matrix, leading to relatively slower release. The dielectric loss and the permittivity can also be correlated with the ionic interactions with water and the mobility of water molecules in the polymeric particles (dispersed phase), respectively. As per the report published by Henry *et al.*,[92] the hydrated polymeric particles with more bound water molecules due to higher polarity, may exhibit less dielectric loss, but higher permittivity. Consequently, swollen hydrophilic particles (S1) may facilitate the spreading of RF wave and produce less heat as compared to the ones with least swelling (S6). In other words, it can be stated that the rapid spreading of the vibration became easier through the swollen spongy cellulosic core (hydrophilic), which allowed faster ingression of water molecules through the expanded pores, contributing to the rupture of the whole core shell microspheres, thereby expelling the drug (Fig. 10).

The micropshere rupture upon RF exposure was evident from the FESEM analysis (Fig. 9a). Complete disintegration of the microspheres was evident for S1 and S2 samples only, where GO remained in the shell, indicating the ease of RF absorption by GO and its conductance through the swollen cellulosic core. Consequently, a rapid release of drug was realized from these two systems (S1 and S2, Fig. 9a and b respectively) only, implying the impact of the GO location in triggering the drug release. Conversely, when GO was in the core, slower dis-

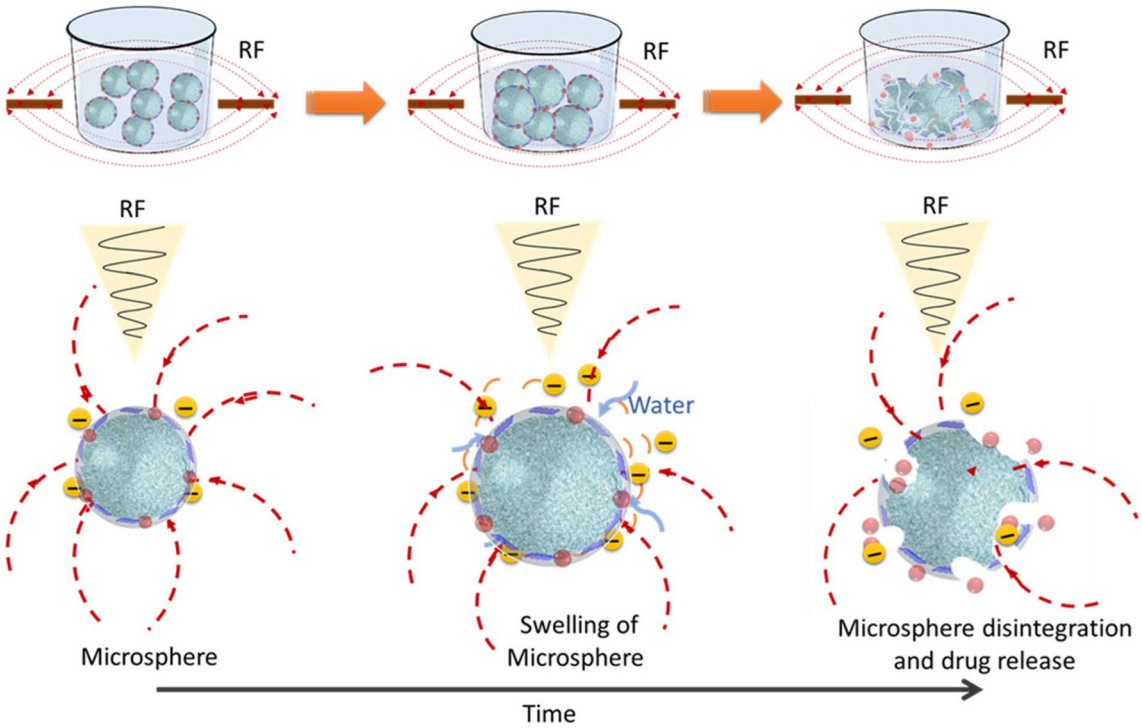

Fig. 10 Schematic representation of the effect of RF on a microsphere.

integration leading to sluggish drug release was observed due to inefficient penetration of electromagnetic field to the embedded GO particles. Moreover, the core–shell morphology of the microspheres certainly facilitated a strong interaction of RF waves with GO, when located in the thin shell of Ac-D (~2 μm, Fig. 1 and 2). The dense packing of GO in the thin Ac-D shell would increase the volumetric density of GO, resulting in improved electrical properties, which may potentially foster a higher interaction with RF waves. On the other hand, GO within the core remained uniformly distributed throughout the porous cellulosic core without forming a percolated network.[93] As a result, a burst release of drug was noticed in the former cases (S1 and S2) only. However, owing to the dense polymeric matrix, the RF-GO interaction was probably less effective when GO was incorporated into Ac-D or PLA microparticles, restricting the penetration and oscillation of RF waves, as reported in literature.[94] Between Ac-D and PLA, former being the relatively more hydrophilic (contact angle of Ac-D: ~50°[95] and PLA: ~80°[96]) as evident from their swelling study (Fig. S14†), Ac-D may show higher permittivity through bound water molecules,[92] which may ease in spreading RF waves in comparison to PLA. Nevertheless, this was not sufficient for rapid drug release, as the dense matrix of Ac-D/PLA also restricted the access of water and RF waves into them. This highlighted the importance of porous cellulosic core in the core–shell structure of the microspheres, which could effectively enable the non-invasive, on-demand drug delivery. Further, cytotoxicity of the microsphere was evaluated by conducting the cell viability study of S1 by MTT assay using HEK293 cells. The microspheres exhibited cytocompatibility at concentrations ranging from 50 to 1000 μg mL^{-1}, as shown in Fig. S16.† The cell viability of ~97% was observed for highest concentration (1000 μg mL^{-1}) affirming their cytocompatibility and thus can be considered safe for normal healthy cells. Therefore, the summary of our investigation proposes that these microspheres could be effectively utilized as a tool for triggered drug delivery applications stimulated by low power RF within a notably short duration of time with an improved cytocompatibility. These microspheres can be administered through methods including topical applications such as creams, gels, or patches. Topical delivery using microsphere offers enhanced drug availability, stability and reduced side effects.

4. Conclusion

In this study, we have demonstrated that radiofrequency (RF) fields can effectively trigger drug release from biopolymer-based core–shell microspheres composed of carboxymethyl cellulose (CMC) and acetalated dextran (Ac-D). These microspheres were fabricated using a double emulsion technique and were co-loaded with nanoscale graphene oxide (GO) serving as the RF-responsive component and curcumin as a model hydrophobic drug. The mechanism of core–shell formation was investigated through *in situ* morphological analysis and interfacial tension measurements between the polymer phases. Raman and XPS analyses confirmed the successful

encapsulation and uniform distribution of both GO and curcumin within the microsphere matrix. The resulting microspheres, composed of biodegradable and biocompatible polysaccharides, exhibited excellent structural stability in physiological environments and achieved drug encapsulation efficiencies greater than 50%. Upon RF stimulation, the GO-loaded microspheres exhibited rapid and controlled drug release, with more than 90% of the drug released within 60 minutes. This release behavior is attributed to GO-mediated localized heating, which induces structural disruption, promotes water penetration, and correlates with a high swelling index (~60–70%) and measurable surface charge differences. Overall, this work highlights the critical role of nanoscale GO as a functional transducer within a microscale delivery system, enabling non-invasive, externally triggered, and spatiotemporally controlled drug delivery. The developed system holds strong potential for real-world biomedical applications particularly in topical formulations such as creams, gels, or patches, where localized and on-demand drug release is desirable. Future work will focus on *in vivo* evaluation and formulation optimization to advance these materials to confirm the long-term safety and biocompatibility of the system, especially for clinical translation.

Data availability

All data are available in the main text or ESI.†

Conflicts of interest

There are no conflicts to declare.

Acknowledgements

SS and AT would like to appreciate the Department of Materials Science and Engineering (DMSE), Indian Institute of Technology (IIT), SERB POWER grant (SPF12023/000021) and Department of Science and Technology (DST) and CRF, IIT Delhi for providing funds, characterization, and research facility. AKB and AV would like to acknowledge the support of the University of Washington, Mechanical Engineering. The authors thank Dr Hemlata, and Prof. Shilpi Minocha from Kusuma School of Biological Sciences, Indian Institute of Technology Delhi for helping authors in conducting cytocompatibility test.

References

1 S. Adepu and S. Ramakrishna, *Molecules*, 2021, **26**, 5905.
2 S. Ganta, A. Singh, T. P. Coleman, D. Williams and M. Amiji, in *Nanomedicine*, ed. Y. Ge, S. Li, S. Wang and R. Moore, Springer New York, New York, NY, 2014, pp. 191–236.
3 Z. Jiang, H. Jin, S. Sun, C. Chen, J. Zhang, Z. Guo and X. Liu, *Mater. Sci. Eng., C*, 2018, **93**, 846–852.
4 S. S. Pradhan and S. Saha, *Adv. Colloid Interface Sci.*, 2022, **300**, 102580.
5 I. Mirza and S. Saha, *ACS Appl. Bio Mater.*, 2020, **3**, 8241–8270.
6 S. Dutta, N. Shreyash, B. K. Satapathy and S. Saha, *Wiley Interdiscip. Rev.: Nanomed. Nanobiotechnol.*, 2023, **15**, e1861.
7 K. Park, *J. Controlled Release*, 2014, **190**, 3–8.
8 D. Liu, F. Yang, F. Xiong and N. Gu, *Theranostics*, 2016, **6**, 1306–1323.
9 N. Gupta, P. K. Sharma, S. S. Yadav, M. Chauhan, A. K. Datusalia and S. Saha, *ACS Biomater. Sci. Eng.*, 2024, **10**, 5039–5056.
10 M. Liu, H. Du, W. Zhang and G. Zhai, *Mater. Sci. Eng., C*, 2017, **71**, 1267–1280.
11 P. Vinchhi, S. U. Rawal and M. M. Patel, in *Drug Delivery Devices and Therapeutic Systems*, Elsevier, 2021, pp. 267–288.
12 S. Mura, J. Nicolas and P. Couvreur, *Nat. Mater.*, 2013, **12**, 991–1003.
13 A. V. Andriyanov, E. Koren, Y. Barenholz and S. N. Goldberg, *PLoS One*, 2014, **9**, e92555.
14 M. Bariana, M. S. Aw, E. Moore, N. H. Voelcker and D. Losic, *Nanomedicine*, 2014, **9**, 1263–1275.
15 M. A. Rahim, N. Jan, S. Khan, H. Shah, A. Madni, A. Khan, A. Jabar, S. Khan, A. Elhissi, Z. Hussain, H. C. Aziz, M. Sohail, M. Khan and H. E. Thu, *Cancers*, 2021, **13**, 670.
16 C. S. Linsley and B. M. Wu, *Ther. Delivery*, 2017, **8**, 89–107.
17 L. Wang, P. Zhang, J. Shi, Y. Hao, D. Meng, Y. Zhao, Y. Yanyan, D. Li, J. Chang and Z. Zhang, *ACS Appl. Mater. Interfaces*, 2015, **7**, 5736–5747.
18 Y. Xu, A. Karmakar, W. E. Heberlein, T. Mustafa, A. R. Biris and A. S. Biris, *Adv. Healthcare Mater.*, 2012, **1**, 493–501.
19 R. Kumar, A. Chauhan, S. K. Jha and B. K. Kuanr, *J. Mater. Chem. B*, 2018, **6**, 5385–5399.
20 A. Sasidharan, S. Swaroop, C. K. Koduri, C. M. Girish, P. Chandran, L. S. Panchakarla, V. H. Somasundaram, G. S. Gowd, S. Nair and M. Koyakutty, *Carbon*, 2015, **95**, 511–524.
21 Z. Liu, J. T. Robinson, X. Sun and H. Dai, *arXiv*, 2008, preprint,DOI: 10.48550/ARXIV.0807.4959.
22 K. Yang, S. Zhang, G. Zhang, X. Sun, S.-T. Lee and Z. Liu, *Nano Lett.*, 2010, **10**, 3318–3323.
23 L. Zhang, Z. Lu, Q. Zhao, J. Huang, H. Shen and Z. Zhang, *Small*, 2011, **7**, 460–464.
24 F. Valentini, E. Mari, A. Zicari, A. Calcaterra, M. Talamo, M. G. Scioli, A. Orlandi and S. Mardente, *Int. J. Mol. Sci.*, 2018, **19**, 1316.
25 A. Sasidharan, A. J. Sivaram, A. P. Retnakumari, P. Chandran, G. L. Malarvizhi, S. Nair and M. Koyakutty, *Adv. Healthcare Mater.*, 2015, **4**, 679–684.
26 A. Sasidharan, L. S. Panchakarla, A. R. Sadanandan, A. Ashokan, P. Chandran, C. M. Girish, D. Menon, S. V. Nair, C. N. R. Rao and M. Koyakutty, *Small*, 2012, **8**, 1251–1263.

27 S. K. Singh, M. K. Singh, M. K. Nayak, S. Kumari, S. Shrivastava, J. J. A. Grácio and D. Dash, *ACS Nano*, 2011, **5**, 4987–4996.
28 V. H. Somasundaram, R. Pillai, G. Malarvizhi, A. Ashokan, S. Gowd, R. Peethambaran, S. Palaniswamy, A. Unni, S. Nair and M. Koyakutty, *ACS Biomater. Sci. Eng.*, 2016, **2**, 768–779.
29 O. M. Andrade, *MRS Proc.*, 1990, **189**, 27.
30 J. T. Leith, R. C. Miller, E. W. Gerner and M. L. M. Boone, *Cancer*, 1977, **39**, 766–779.
31 J. Fang, Y. Yang, W. Xiao, B. Zheng, Y.-B. Lv, X.-L. Liu and J. Ding, *Nanoscale*, 2016, **8**, 3259–3263.
32 X. L. Chang, P. S. Chee, E. H. Lim and W. C. Chong, *Smart Mater. Struct.*, 2019, **28**, 015024.
33 K.-H. Liao, Y.-S. Lin, C. W. Macosko and C. L. Haynes, *ACS Appl. Mater. Interfaces*, 2011, **3**, 2607–2615.
34 B. Fadeel, C. Bussy, S. Merino, E. Vázquez, E. Flahaut, F. Mouchet, L. Evariste, L. Gauthier, A. J. Koivisto, U. Vogel, C. Martín, L. G. Delogu, T. Buerki-Thurnherr, P. Wick, D. Beloin-Saint-Pierre, R. Hischier, M. Pelin, F. Candotto Carniel, M. Tretiach, F. Cesca, F. Benfenati, D. Scaini, L. Ballerini, K. Kostarelos, M. Prato and A. Bianco, *ACS Nano*, 2018, **12**, 10582–10620.
35 A. K. Biswal, A. T. Thodikayil and S. Saha, *ACS Appl. Bio Mater.*, 2021, **4**, 2429–2441.
36 A. T. Thodikayil, A. Yadav, P. Hariprasad and S. Saha, *Int. J. Biol. Macromol.*, 2024, **254**, 127604.
37 P. Prasher, M. Sharma, M. Mehta, S. Satija, A. A. Aljabali, M. M. Tambuwala, K. Anand, N. Sharma, H. Dureja, N. K. Jha, G. Gupta, M. Gulati, S. K. Singh, D. K. Chellappan, K. R. Paudel, P. M. Hansbro and K. Dua, *Colloid Interface Sci. Commun.*, 2021, **42**, 100418.
38 A. Amalin Kavitha, K. Thomas Paul and P. Anilkumar, in *Sustainable Nanocellulose and Nanohydrogels from Natural Sources*, Elsevier, 2020, pp. 367–390.
39 K. Madhusudana Rao, A. Kumar and S. S. Han, *Int. J. Biol. Macromol.*, 2017, **101**, 165–171.
40 S. Mangalathillam, N. S. Rejinold, A. Nair, V.-K. Lakshmanan, S. V. Nair and R. Jayakumar, *Nanoscale*, 2012, **4**, 239–250.
41 E. Einafshar, H. Javid, H. Amiri, H. Akbari-Zadeh and S. I. Hashemy, *Carbohydr. Polym.*, 2024, **340**, 122328.
42 S. K. Yadava, S. M. Basu, R. Valsalakumari, M. Chauhan, M. Singhania and J. Giri, *ACS Appl. Bio Mater.*, 2020, **3**, 6811–6822.
43 J. Tuček, P. Błoński, J. Ugolotti, A. K. Swain, T. Enoki and R. Zbořil, *Chem. Soc. Rev.*, 2018, **47**, 3899–3990.
44 C. Chung, Y.-K. Kim, D. Shin, S.-R. Ryoo, B. H. Hong and D.-H. Min, *Acc. Chem. Res.*, 2013, **46**, 2211–2224.
45 B. Chen, M. Liu, L. Zhang, J. Huang, J. Yao and Z. Zhang, *J. Mater. Chem.*, 2011, **21**, 7736.
46 P. M. Peiris, L. Bauer, R. Toy, E. Tran, J. Pansky, E. Doolittle, E. Schmidt, E. Hayden, A. Mayer, R. A. Keri, M. A. Griswold and E. Karathanasis, *ACS Nano*, 2012, **6**, 4157–4168.
47 O. Navrátil, D. Lizoňová, K. Slonková, L. Mašková, A. Zadražil, D. Sedmidubský and F. Štěpánek, *Colloids Surf., B*, 2022, **217**, 112618.
48 S. A. Malekar, A. L. Sarode, A. C. Bach, A. Bose, G. Bothun and D. R. Worthen, *AAPS PharmSciTech*, 2015, **16**, 1335–1343.
49 Y.-J. Wang, M.-H. Pan, A.-L. Cheng, L.-I. Lin, Y.-S. Ho, C.-Y. Hsieh and J.-K. Lin, *J. Pharm. Biomed. Anal.*, 1997, **15**, 1867–1876.
50 R. Ravichandran, *Adv. Nanopart.*, 2013, **02**, 51–59.
51 H. Kharkwal, K. Bala, D. Joshi and D. P. Katare, *Pharm. Lett.*, 2012, **4**, 1698–1711.
52 E. M. Bachelder, E. N. Pino and K. M. Ainslie, *Chem. Rev.*, 2017, **117**, 1915–1926.
53 H. Ji, Z. Xiang, H. Qi, T. Han, A. Pranovich and T. Song, *Green Chem.*, 2019, **21**, 1956–1964.
54 J. Chen, Y. Li, L. Huang, C. Li and G. Shi, *Carbon*, 2015, **81**, 826–834.
55 A. Sawant, S. Kamath, H. Kg and G. P. Kulyadi, *AAPS PharmSciTech*, 2021, **22**, 199.
56 R. Bodmeier and J. W. McGinity, *Pharm. Res.*, 1987, **04**, 465–471.
57 C. B. Braga, L. A. Kido, E. N. Lima, C. A. Lamas, V. H. A. Cagnon, C. Ornelas and R. A. Pilli, *ACS Biomater. Sci. Eng.*, 2020, **6**, 2929–2942.
58 A. K. Biswal, M. Usmani, S. Z. Ahammad and S. Saha, *J. Mater. Sci.*, 2018, **53**, 5942–5957.
59 E. J. Pollauf and D. W. Pack, *Biomaterials*, 2006, **27**, 2898–2906.
60 A. K. Biswal and S. Saha, *J. Colloid Interface Sci.*, 2020, **566**, 120–134.
61 S. Sharma, S. S. Pradhan, N. Gupta, S. Mondal, D. Ghosal, S. Kumar, M. J. Swamy and S. Saha, *Polymer*, 2024, **308**, 127324.
62 C. E. Rapier, K. J. Shea and A. P. Lee, *Sci. Rep.*, 2021, **11**, 14512.
63 P. Laurent, P. Vanderbemden, S. Meslin, J. G. Noudem, J.-P. Mathieu, R. Cloots and M. Ausloos, *IEEE Trans. Appl. Supercond.*, 2007, **17**, 3036–3039.
64 P. Costa and J. M. Sousa Lobo, *Eur. J. Pharm. Sci.*, 2001, **13**, 123–133.
65 P. Kumar, A. Nagarajan and P. D. Uchil, *Cold Spring Harbor Protoc.*, 2018, **2018**, pdb.prot095505.
66 S. Wang, F. Fontana, M.-A. Shahbazi and H. A. Santos, *Chem. Commun.*, 2021, **57**, 4212–4229.
67 Z. Lin, J. Li, H. He, H. Kuang, X. Chen, Z. Xie, X. Jing and Y. Huang, *RSC Adv.*, 2015, **5**, 9546–9555.
68 E. M. Bachelder, T. T. Beaudette, K. E. Broaders, J. Dashe and J. M. J. Fréchet, *J. Am. Chem. Soc.*, 2008, **130**, 10494–10495.
69 L. Cui, J. L. Cohen, C. K. Chu, P. R. Wich, P. H. Kierstead and J. M. J. Fréchet, *J. Am. Chem. Soc.*, 2012, **134**, 15840–15848.
70 M. Malani, A. T. Thodikayil, S. Saha and J. Nirmal, *Carbohydr. Polym.*, 2024, **324**, 121558.

71 X. Cao, W. Li, T. Ma and H. Dong, *RSC Adv.*, 2015, **5**, 79969–79975.
72 R. S. Van Der Kooij, R. Steendam, H. W. Frijlink and W. L. J. Hinrichs, *Eur. J. Pharm. Biopharm.*, 2022, **170**, 24–42.
73 E. C. Tan, R. Lin and C.-H. Wang, *J. Colloid Interface Sci.*, 2005, **291**, 135–143.
74 J. Liu, L. Cui and D. Losic, *Acta Biomater.*, 2013, **9**, 9243–9257.
75 N. S. Rejinold, R. Jayakumar and Y.-C. Kim, *J. Controlled Release*, 2015, **204**, 85–97.
76 D. Debnath, X. Zhao, M. Anas, D. L. Kulhanek, J. H. Oh and M. J. Green, *Carbon*, 2020, **169**, 475–481.
77 H. Wu, H. Shi, Y. Wang, X. Jia, C. Tang, J. Zhang and S. Yang, *Carbon*, 2014, **69**, 379–389.
78 M. Kashif, E. Jafaar, S. K. Sahari, F. W. Low, N. D. Hoa, A. Ahmad, A. Abbas, Z. Ngaini, M. Shafa and A. Qurashi, *Int. J. Energy Res.*, 2021, **45**, 9657–9666.
79 K. Hatakeyama, M. R. Karim, C. Ogata, H. Tateishi, A. Funatsu, T. Taniguchi, M. Koinuma, S. Hayami and Y. Matsumoto, *Angew. Chem., Int. Ed.*, 2014, **53**, 6997–7000.
80 A. P. P. Alves, L. P. Z. De Oliveira, A. A. N. Castro, R. Neumann, L. F. C. De Oliveira, H. G. M. Edwards and A. C. Sant'Ana, *Vib. Spectrosc.*, 2016, **86**, 324–330.
81 Z. Shaterabadi, G. Nabiyouni and M. Soleymani, *Mater. Sci. Eng., C*, 2017, **75**, 947–956.
82 Y. Li, Y. Xu, T. Zhou, A. Zhang and J. Bao, *RSC Adv.*, 2015, **5**, 32469–32478.
83 M. J. Li, C. M. Liu, H. B. Cao and Y. Zhang, *Adv. Mater. Res.*, 2013, **716**, 127–131.
84 M. Lotya, Y. Hernandez, P. J. King, R. J. Smith, V. Nicolosi, L. S. Karlsson, F. M. Blighe, S. De, Z. Wang, I. T. McGovern, G. S. Duesberg and J. N. Coleman, *J. Am. Chem. Soc.*, 2009, **131**, 3611–3620.
85 T. V. Patil, D. K. Patel, S. D. Dutta, K. Ganguly and K.-T. Lim, *Molecules*, 2021, **26**, 2797.
86 E. Chibowski, L. Hołysz and W. Wójcik, *Colloids Surf., A*, 1994, **92**, 79–85.
87 A. K. Biswal, I. Vashisht, A. Khan, S. Sharma and S. Saha, *J. Mater. Sci.*, 2019, **54**, 9745–9758.
88 F. Carrasco, O. Santana Pérez and M. Maspoch, *Polymers*, 2021, **13**, 3996.
89 L. Szcześniak, A. Rachocki and J. Tritt-Goc, *Cellulose*, 2008, **15**, 445–451.
90 K. J. Hodgetts and T. W. Wallace, *Synth. Commun.*, 1994, **24**, 1151–1155.
91 D. M. P. Mingos and D. R. Baghurst, *Chem. Soc. Rev.*, 1991, **20**, 1.
92 F. Henry, C. Pichot, A. Kamel and M. S. El Aasser, *Colloid Polym. Sci.*, 1989, **267**, 48–58.
93 Z. Barani, F. Kargar, K. Godziszewski, A. Rehman, Y. Yashchyshyn, S. Rumyantsev, G. Cywiński, W. Knap and A. A. Balandin, *ACS Appl. Mater. Interfaces*, 2020, **12**, 28635–28644.
94 N. Gill, A. L. Sharma, V. Gupta, M. Tomar, O. P. Pandey and D. P. Singh, *J. Alloys Compd.*, 2019, **797**, 1190–1197.
95 N. Chen, M. A. Collier, M. D. Gallovic, G. C. Collins, C. C. Sanchez, E. Q. Fernandes, E. M. Bachelder and K. M. Ainslie, *Int. J. Pharm.*, 2016, **512**, 147–157.
96 S. Dhingra, V. Gaur, J. Bhattacharya and S. Saha, *J. Mater. Chem. B*, 2023, **11**, 83–98.

